JOURNAL OF GEOPHYSICAL RESEARCH, VOL. 106, NO. D14, PAGES 15,099–15,112, JULY 27, 2001

Modeling with explicit spectral water and ice microphysics of a two-layer cloud system of altostratus and cirrus observed during the FIRE Arctic Clouds Experiment

V. I. Khvorostyanov, J. A. Curry, J. O. Pinto

Department of Aerospace Engineering Sciences, University of Colorado, Boulder, Colorado

M. Shupe

Science and Technology Corporation, NOAA Environmental Technology Laboratory, Boulder, Colorado

B.A. Baker

SPEC, Inc., Boulder, Colorado

K. Sassen

Meteorology Department, University of Utah, Salt Lake City, Utah

Abstract. A one-dimensional version of a cloud model with an explicit microphysics scheme is used to simulate a case study of middle and upper level cloud formation and evolution that was observed during the FIRE Arctic Clouds Experiment. In the simulations, the midlevel altostratus cloud is initially liquid phase, then partially freezes, and exists in mixed phase for several hours with a relative equilibrium between the rate of drop production by condensation and their depletion by freezing. The dominant mode of cirrus formation was periodic homogeneous freezing of deliquescent submicron haze particles. These crystal layers form near the tropopause and, subsequently, precipitate into the middle troposphere, causing seeding of the underlying altostratus cloud. Sensitivity tests are conducted varying the initial humidity and nucleation schemes.

1. Introduction

The importance of Arctic clouds and radiation on the regional and global climate is summarized by *Curry et al.* [1996]. Difficulty in simulating and remotely sensing these clouds motivated the FIRE Arctic Clouds Experiment [*Curry et al.*, 2000], which was conducted in conjunction with the Surface Heat Budget of the Arctic Ocean (SHEBA) experiment [*Perovich et al.*, 1999]. The problems in modeling Arctic clouds have been hypothesized by *Curry et al.* [1996] to arise from the complex vertical structure of the stable arctic atmosphere, the presence of mixed phase clouds, and the susceptibility of the Arctic clouds to modification by aerosol.

Curry et al. [2000] describe an initial application of the SHEBA/FIRE data set to evaluating cloud parameterizations in the context of single-column model simulations. Results of simulations for May 1998 showed that the models tend to underpredict low cloud amount and the column liquid water path. The underprediction of the column liquid water path was in part attributed to inaccurately representing mixed phase clouds as entirely crystalline.

Mixed-phase clouds occur at high frequency in the Arctic from September to June [Pinto, 1998; *Curry et al.*, 1990, *Perovich et al.*, 1999; *Pinto et al.*, this issue]. From observations obtained during autumn from the Beaufort Arctic Storms Experiment (BASE), *Pinto* [1998] hypothesized that mixed-phase clouds are maintained in the Arctic boundary layer through a balance of condensation of liquid water through cooling and heterogeneous freezing of the cloud drops. *Jiang et al.* [2000] simulated the case study described by Pinto and found strong sensitivity of the phase of the cloud to the concentration of ice-forming nuclei (IFN). Simulations by *Girard and Blanchet* [2000] have shown that low-level clouds may remain in a mixed-phase state as long as 10 hours in the Arctic during winter.

Most of the focus on Arctic clouds has been on boundary layer stratus, which were shown by *Curry et al.* [1993] to have the greatest influence on the surface radiation balance and the ice-albedo feedback in the Arctic. Relatively little attention has been paid to altostratus and cirrus in the Arctic, largely because of the difficulties in observing these clouds from satellite, especially during the polar night. The importance of cirrus clouds in the Arctic arises from their impact on the radiation balance. Additionally, seeding of low-level clouds by upper level crystalline clouds [e.g., *Hobbs and Rangno*, 1998] appears to be an important mechanism for the phase transition of boundary layer clouds. Observations [e.g., *Curry et al.*, 1996] show that mixed-phase clouds can persist in the Arctic at temperatures as low as -32°C, presumably because of the general paucity of IFN.

During BASE in autumn 1994, some aircraft observations of altostratus and cirrus were obtained. J. Intrieri (personal communication, 1996) examined cirrus clouds with temperatures between -19° and -42°C and found that the Arctic

Paper number 2000JD900521.
0148-0227/01/2000JD900521$09.00

cirrus had microphysical properties similar to middle and low-latitude cirrus. The mean properties of cirrus observed during BASE are reported by *Pinto et al.* [this issue]. The cirrus observed in autumn over the Beaufort Sea occurred between 4 and 7 km, much lower than the mean heights of wintertime midlatitude cirrus (9500 in) and tropical cirrus (12500 in). Because of their lower heights, Arctic cirrus is generally warmer than middle and low-latitude cirrus. The warmer temperature of the Arctic cirrus clouds is associated with the low tropopause (below 10 km), which typically has a minimum temperature of -60°C. Hence cirrus clouds in the Arctic are relatively warm, suggesting that ice nucleation mechanisms might be different for the Arctic cirrus than for low-latitude cirrus that forms at colder temperatures. This is further suggested by the findings of *Korolev et al.* [1999] during the FIRE Arctic Clouds Experiment, who found that particle shapes of middle and high-level clouds were predominantly irregular over the temperature range -20° to -45°C.

Analyzing lidar and aircraft data in midlatitude cirrus, *Sassen and Dodd* [1988, 1989] hypothesized that the main mechanism of cirrus formation for midlatitude conditions is homogeneous crystal nucleation by the freezing of deliquescent hygroscopic aerosol. This process proceeds as periodic "microbursts" of nucleation, separated by the absence of crystal formation due to the strong negative feedback between crystal concentration and ice supersaturation. The various schemes of ice nucleation in cirrus formation have been studied also by *Heymsfileld and Sabin* [1989], *DeMott et al.* [1994], *Jensen et al.* [1994], and *Khvorostyanov and Sassen* [1998a, 1998b, 1998c, 2000; hereinafter referred to as KS98a, KS98b, KS98c, KS00].

Bulk microphysical parameterizations used in climate models [e.g., *Fowler et al.*, 1996] typically distinguish the phase of cloud water by the cloud temperature. The discrimination between the liquid and ice phases may be specified in terms of a single cutoff temperature or as a function of temperature with the ratio of ice water content to total water content varying from 0 at 0°C to 1 at -40°C. *Curry et al.* [1996] cite observations of liquid drops in Arctic clouds at temperatures as low as -32°C, and clouds that are completely glaciated at -14°C. Clearly, a simple temperature-phase relationship is not sufficient to diagnose the phase of supercooled clouds in the Arctic. IFN concentration and composition are factors, as well as the size of liquid drops in heterogeneous freezing, ice nucleation mechanism, and secondary ice production processes. *Girard and Curry* [this issue] have developed a bulk microphysics scheme for Arctic clouds that also includes prognostic variables for liquid and ice particle concentration and cloud supersaturation, which interacts with a specified atmospheric aerosol. While the Girard-Curry parameterization provides more degrees of freedom for cloud microphysical properties and cloud phase, there remain numerous uncertainties in the parameterization of many relevant microphysical processes.

Explicit microphysics, which resolves the particle size distribution and its evolution, allows more precise evaluation of the particle size spectra and supersaturation budget. In this paper, we use a one-dimensional version of a cloud model with explicit microphysics *[Khvorostyanov,* 1995 (hereinafter referred to as K95); KS98a, KS00] to simulate a case study of the two-layer cloud system consisting of As and Ci observed on July 8, 1998, during the FIRE Arctic Clouds Experiment. We adopt the general single-column modeling strategy described by *Randall et al.* [1996] and *Randall and Cripe* [1999], using the European Centre for Medium-Range Weather Forecasting (ECMWF) analyses to provide advective tendencies, and using field observations to provide the initial conditions and evaluation data. The objectives of this study are to (1) test the feasibility of the single-column modeling strategy for evaluating an explicit microphysics scheme against observations, (2) use the simulations to interpret physical processes occurring in the cloud, and (3) assess the sensitivity of the formation of the upper level clouds to the initial atmospheric humidity and ice nucleation schemes.

2. Observations

An overview of the FIRE Arctic Clouds Experiment is given by *Curry et al.* [2000], and SHEBA is described by *Perovich et al.* [1999]. An icebreaker ship drifted in the Beaufort/Chukchi Seas during the period October 1997 through October 1998, serving as the central platform for the SHEBA ice station from which surface-based measurements were made. During April through July 1998, research aircraft overflights of the SHEBA ice camp were made, making in situ measurements of the atmosphere and remote measurements of the surface.

Observational data sets employed in this study include in situ microphysical observations from aircraft, surface-based cloud radar, microwave radiometer observations, and radiosonde temperature and humidity profiles. Boundary advection and vertical velocity profiles are obtained from forecasts of the European Center for Medium Range Weather Forecasting (ECMWF) numerical weather prediction model. The millimeter cloud radar (35 GHz, Ka band) is a vertically pointing Doppler system that provides estimates of reflectivity, mean vertical velocity, and spectral width at each gate over a height range of 0.1 to 13 km above the surface. Retrievals of cloud microphysical properties from the radar and microwave radiometer data for SHEBA are described by Shupe et al. [this issue] following the method of Matrosov et al. [1994]. The microwave radiometer consists of two channels (23.8 and 31.4 GHz) which allows for the simultaneous determination of precipitable water and liquid water path [*Liljegren*, 1999]. In situ measurements of cloud ice were obtained with the SPEC Cloud Particle Imager (CPI) and the PMS (Particle Measuring System) 260x probe which were flown on the NCAR C-130. The CPI probe produces high-resolution digital images of particles as they pass through the instrument sample volume. The high resolution images can be used to distinguish small ice particles from liquid drops in mixed-phase clouds. and to estimate the ice water content [*Lawson et al.*, this issue]. Specification of atmospheric aerosol characteristics were guided by the measurements described by *Yum and Hudson* [this issue] and *Rogers et al.* [this issue].

The case study examined here occurred on July 8, 1998, over the SHEBA ice camp in the Chukchi Sea. A large high-pressure system occupied the Chukchi and Beaufort Seas. The SHEBA ship was on the north side of this high with westerly winds. A trajectory analysis shows that the air at 3 km came from Siberia to the southwest, and air at levels between 6 and 9 km came from central Asia, farther west. From 0000 to 0300 UTC, a deep cloud system with some precipitation was present, with radar echoes from the surface to 6 km (Plate 1). The cloud became increasingly broken from 0530 to 1000. An

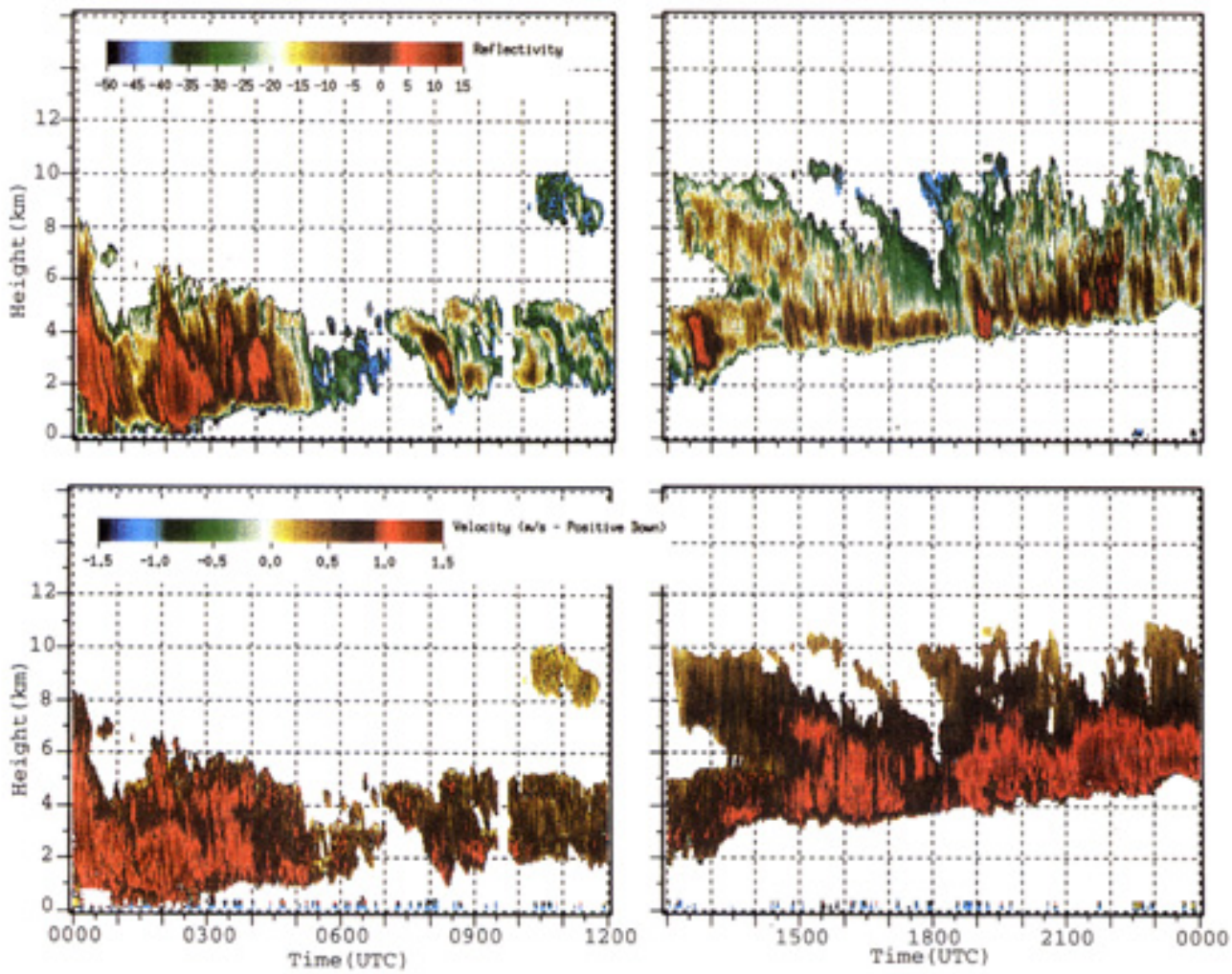

Plate 1. Time-height display of radar observations at the Surface Heat Budget of the Arctic Ocean (SHEBA) site on July 8, 1998: (a) radar reflectivity (dBz), (b) Doppler fall velocities (in s^{-1}).

upper cloud appeared in the radar image at 1100, with temperature around -55°C, and merged with the lower cloud (temperature -10° to -20°C at 1330 UTC). The base of lower cloud gradually elevated between 1200 and 2400 UTC, with cloud base increasing from 2 to 5 km. Some liquid water was present (as inferred from the microwave radiometer), the amount diminishing to almost nothing after 1500 UTC.

Figure 1 shows a comparison of ice crystal microphysical properties observed by both the radar and the CPI. The radar retrievals were obtained over the period 2130 to 2230 UTC, following *Matrasov et al* [1994]. The median values are shown along with values at the first and third quartiles. The CPI data were obtained from a single aircraft profile during the period 2123-2126 UTC. The CPI IWC values tend to be much smaller (i.e., an order of magnitude) than the radar retrieved values. The mean CPI ice water content (IWC) is similar to the first quartile estimates from the radar data (Figure 1a) while the maximum CPI values match the radar median values. The mean CPI concentrations generally range between 300 and 400 L^{-1} well above cloud base (Figure 1b) with 90% of the particles being less than 25 microns in diameter. Ice crystal sizes observed with the CPI probe and retrieved from radar data are shown in Figure 1c. The range of CPI values indicates the bin sizes that had concentrations greater than 1 L^{-1}. The mean radius of the CPI ice particles was around 10 μm through the portion of the cloud sampled by aircraft; however, larger crystals with radii of up to 35 μm were detected at concentration greater than 1 L^{-1} toward cloud base. These mean sizes obtained with the CPI probe are likely much smaller than the actual mean cloud particle size because the CPI under samples the larger ice crystals. In situ data collected with the 260x probe, which is sensitive to larger cloud particle sizes, revealed that cloud particles with radii as large as 170 μm were present at concentrations greater than 1 L^{-1} (not shown). The radar-retrieved values tend to be much larger than the CPI values with median values at the aircraft levels of 40 to 70 μm. The radar retrieval clearly indicates that the ice crystal size decreases with height through the cloud layer.

The large differences between the CPI and radar indicate that the two measurements give vastly different information about the cloud properties. The radar data are dominated by the sixth power dependence on particles size, are representative of the cloud scale, and may not adequately reflect the presence of small ice particles. The in situ CPI data are representative of the cloud microscale and the probe has its greatest sensitivity at the smaller end of the particle size spectrum. Further analysis of in situ data collected by CPI and other microphysical probes on the aircraft is needed to improve the determination of

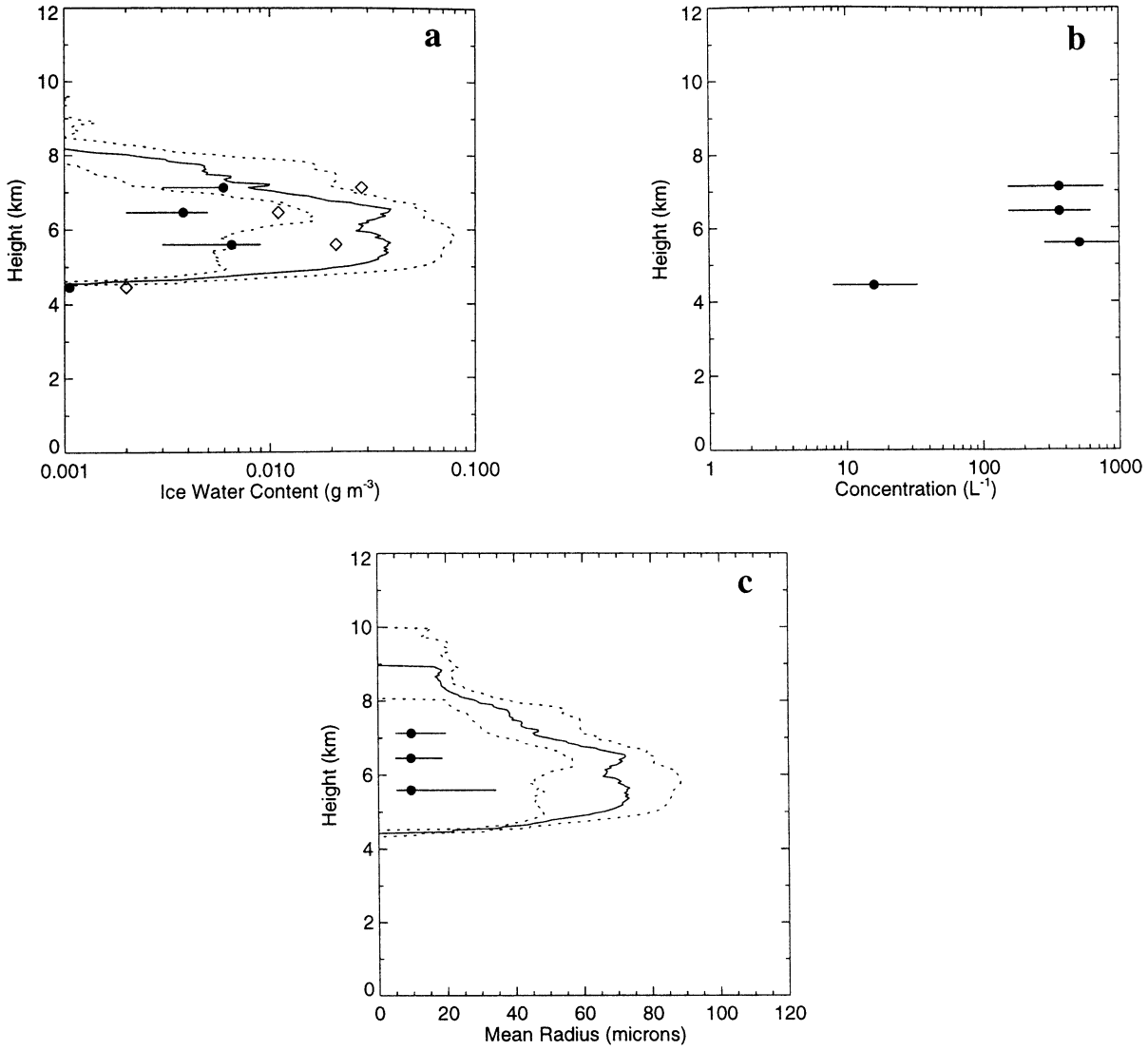

Figure 1. Observed profiles of ice crystal microphysical properties obtained on July 8, 1998, at the SHEBA site, from the cloud radar retrievals (solid curve represents median value; dotted curves represent first and third quartiles for the period 2100-2200 UTC; diamonds represent maximum IWC obtained with the CPI probe during the leg) and the Cloud Particle Imager (circles, obtained around 2130 UTC): (a) ice water content, (b) ice particle concentration, and (c) ice crystal mean radius.

cloud microphysical properties and to relate the scale of the aircraft observations to that of the model and radar.

3. Model Description

The numerical model with explicit water and ice microphysics used in this study has been under development for more than 25 years *[Buikov and Khvorostyanov,* 1976; *Khvorostyanov*, 1982, K95, KS98a, KS00]. The model can be configured as 1-D, 2-D or 3-D, and has been applied to a variety of cloud types (boundary layer stratus, multilayered orographic cloud systems, deep convective clouds, frontal stratiform clouds); a review is given in K95.

For this study, we use the 1-D (single column) version of the model, with the large-scale dynamics specified from ECMWF initialized analyses. The model has been modified for this study in its treatment of aerosol microphysics and ice nucleation (described in the following sections), to specifically address mixed-phase clouds observed in the Arctic.

The 1-D model contains seven basic modules, which are described in the publications listed in the previous paragraph: (1) cloud microphysics (kinetic equations for the droplet and crystal size spectra that describe condensation and aggregation) and thermodynamics (temperature, humidity and supersaturation); (2) transport of cloud condensation nuclei (CCN), ice nuclei (IN), and up to 20 pollutants; (3) formation of the size spectra of deliquescent submicron aerosol; (4) homogeneous and heterogeneous nucleation of crystals; (5) longwave radiation; (6) solar radiation; and (7) heat and moisture exchange with the underlying surface. This model allows detailed calculations of the phase transformations, precipitation, and the optical and radiative characteristics of the simulated clouds. Because of the emphasis of this study on cloud microphysics and thermodynamics, these aspects of the model are described in some detail below.

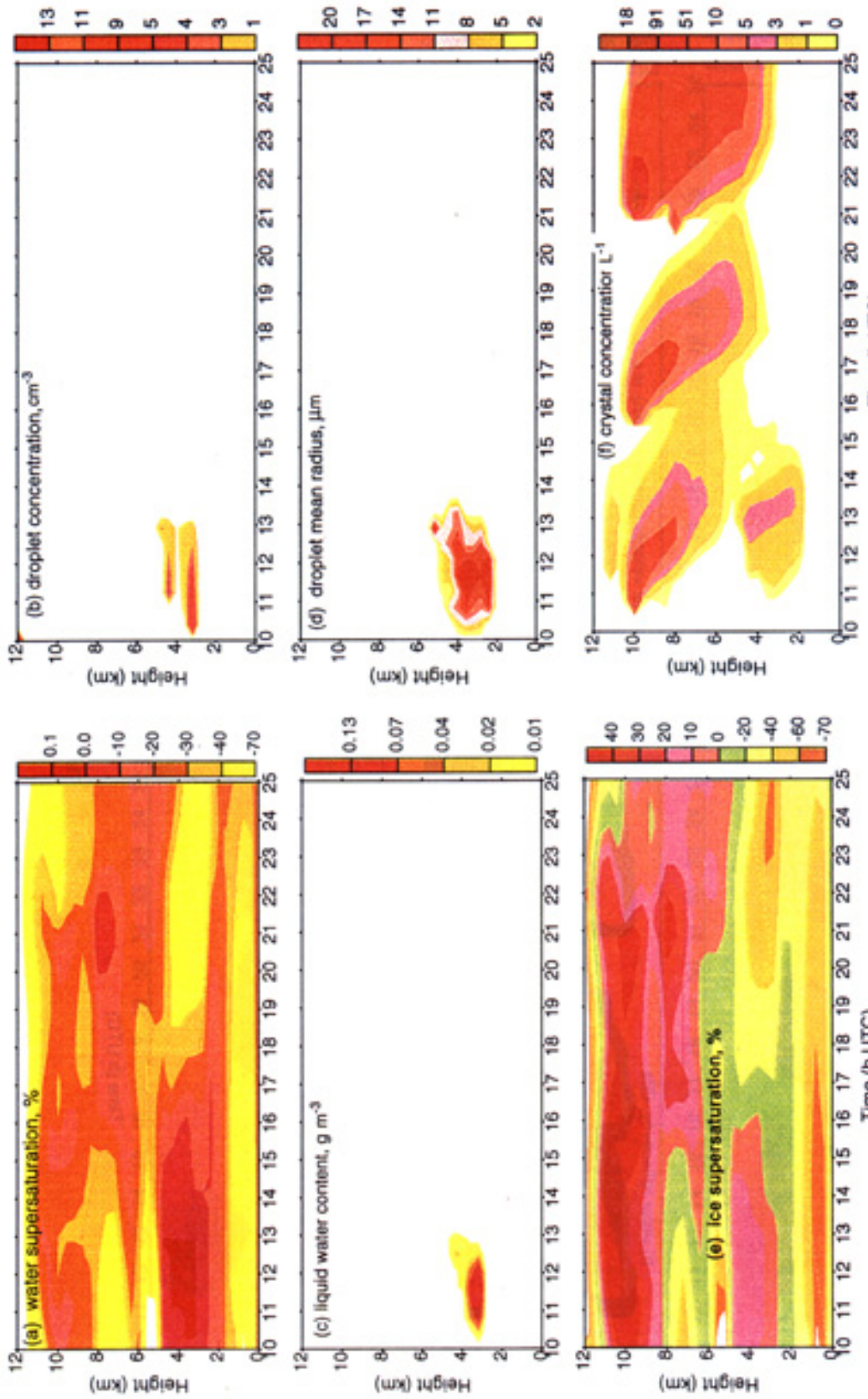

Plate 2. Simulated in the control run cloud evolution from zero to 2200 UTC. First sheet: (a) water supersaturation, %; (b) droplet concentration, cm^{-3}; (c) liquid water content, g m^{-3}; (d) droplet mean radius, μm; (e) ice supersaturation, %; (f) crystal concentration, L^{-1}; (g) ice water content, mg m^{-3}; (h) crystal mean radius, μm: (i) radar reflectivity, dBz; (j) fall (Doppler) velocity, in s^{-1}; (k) crystal supersaturation relaxation time, min; (l) relative amount of condensed ice, RACI, %.

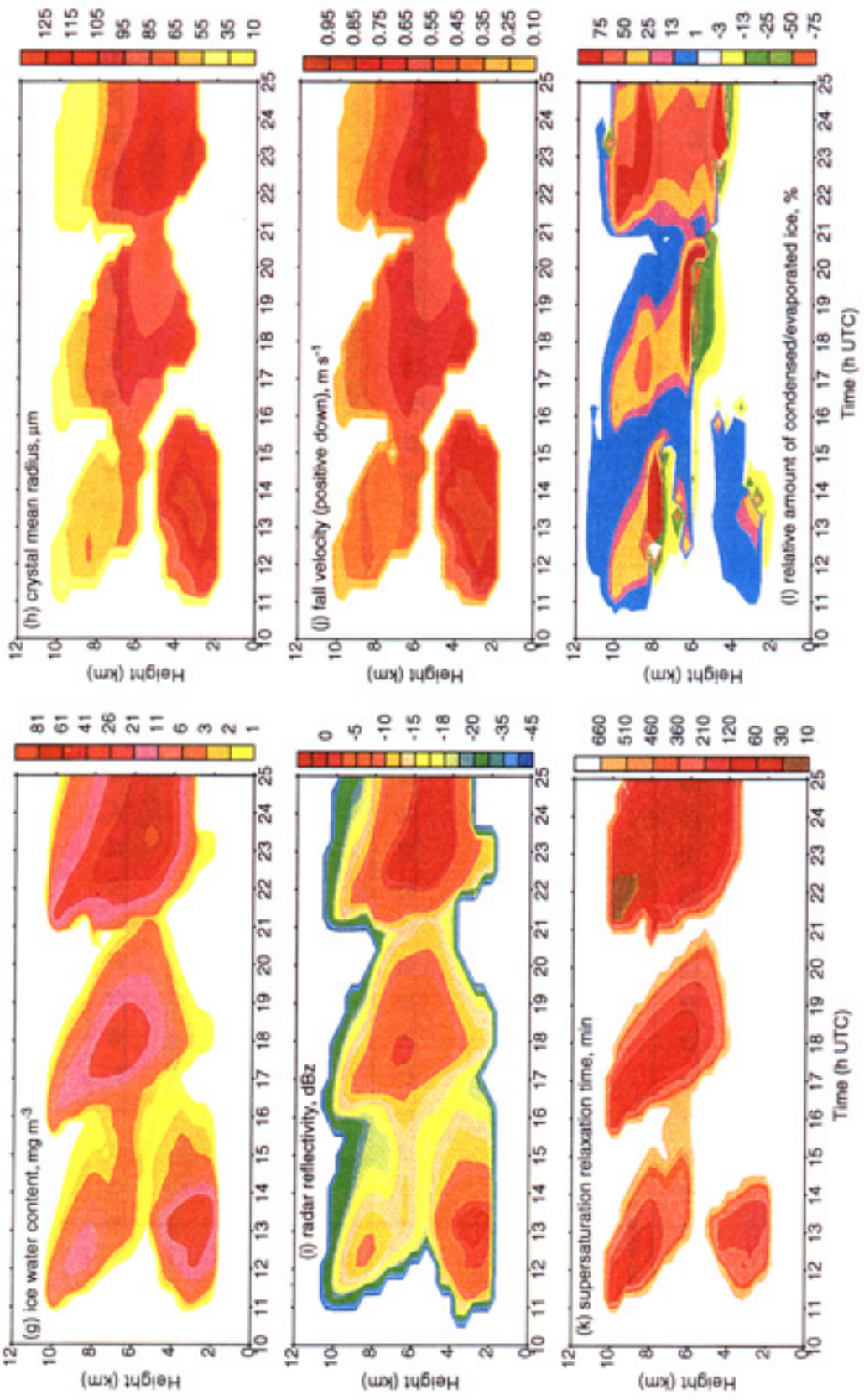
(g) ice water content, mg m-3
(h) crystal mean radius, μm
(i) radar reflectivity, dBz
(j) fall velocity (positive down), m s-1
(k) supersaturation relaxation time, min
(l) relative amount of condensed/evaporated ice, %
Height (km)
Time (h UTC)

3.1. Particle Size Spectra

Spectra of the drop and crystal sizes are determined using kinetic theory. We describe the droplet size spectra using the size distribution function following *Khvorostyanov and Curry* [1999a (hereinafter referred to as KC99a)]. The crystal size spectra are described following KS98a. We approximate ice crystal size using the radius of the volume-equivalent sphere. The kinetic equations for the particle size distribution functions $f(z, t, r)$ can be written as (hereinafter i = 1 denotes droplets and i = 2 denotes crystals)

$$\frac{\partial f_i(z,r,r_i)}{\partial t}+\frac{\partial}{\partial z}\left[w-v_i(r_i)\right]f_i=\frac{\partial}{\partial z}k_z\frac{\partial f_i}{\partial z}+\left(\frac{\partial f_i}{\partial t}\right)_{nucl}-\frac{\partial}{\partial r_i}(\dot{r}_i f_i)$$
$$+\left(\frac{\partial f_i}{\partial t}\right)_{coag}+\left(\frac{\partial f_i}{\partial t}\right)_{freez}+\left(\frac{\partial f_i}{\partial t}\right)_{melt}+\left(\frac{\partial f_i}{\partial t}\right)_{mult} \quad (1)$$

Here z is the vertical coordinate, t is time, r_i is droplet or crystal radius, $v_i(r_i)$ is terminal velocity, k_z is the coefficient of vertical turbulent diffusion, and w is vertical velocity. The last six terms on the right-hand side of (1) describe the following microphysical processes: nucleation, deposition or sublimation, coagulation, freezing, melting, and the multiplication of particles, respectively. These processes are parameterized as described below.

The particle radius growth or evaporation rate is determined following *Pruppacher and Klett* [1997], which includes kinetic and ventilation effects [see also KC99a]. Deposition, sublimation, coagulation, freezing, melting, and the multiplication of particles are parameterized as described by K95, KS98a, and KC99a. Ice nucleation as implemented in this model is described by KS98c and KS00. In this study we examine two different parameterizations of heterogeneous nucleation: *Meyers et al.* [1992, (hereinafter referred to as MDC92)], which parameterizes the number of activated ice particles to be a function of ice supersaturation; and *Fletcher* [1962], which parameterizes the number of activated ice particles to be a function of cloud temperature and altitude (the altitude correction following *Sassen* [1992]). The homogeneous nucleation rate is calculated following KS98c, which includes simple analytical expressions for the size of the critical germ and activation energy for diffusion across the liquid-ice boundary. The nucleation rate expression developed by KS98c is a generalization of the classical homogeneous nucleation theory for three-phase systems, providing a solution to the problem of homogeneous nucleation for haze particles in cirrus, droplets of pure water, and the high supersaturations such as might be found at the initial stage of contrail formation.

After calculating the size distribution functions, many characteristics can be calculated as the integrals (moments) over the size spectra at each grid point and time step: liquid water content, ice water content, total concentration of ice and liquid particles, mean and effective radii, radar and lidar reflectivities, absorption and extinction coefficients, optical thickness and emissivity, and integral terminal velocities.

The size spectra of deliquescent haze is based on the simple analytical aerosol model with account for hygroscopic growth developed by *Khvorostyanov and Curry* [1999b (hereinafter referred to as KC99b)] (in this study, soluble aerosol particles are assumed to be either sulfuric acid or ammonium sulfate).

3.2. Cloud Thermodynamics

The treatment of cloud thermodynamics differs here from previous versions of the model by incorporation of thermodynamics appropriate for mixed-phase clouds. A rigorous treatment of supersaturation in the mixed phase clouds is required for correct evolution of cloud particle phase and size distribution. A derivation of the supersaturation equation suitable for mixed phase clouds, along with its numerical solution, is described below.

The potential temperature θ and specific humidity q are calculated from

$$\frac{\partial\theta}{\partial t}+\frac{\partial w\theta}{\partial z}=\frac{\partial}{\partial z}\left(k_z\frac{\partial w\theta}{\partial z}\right)+\frac{L_i}{c_p}\varepsilon_{ci}+\frac{L_f}{c_p}\varepsilon_m+\left(\frac{\theta}{T}\right)\left(\frac{\partial T}{\partial t}\right)^{rad}+\left(\frac{\partial\theta}{\partial t}\right)_{adv} \quad (2)$$

$$\frac{\partial q}{\partial t}+\frac{\partial wq}{\partial z}=\frac{\partial}{\partial z}\left(k_z\frac{\partial wq}{\partial z}\right)-\varepsilon_{ci}+\left(\frac{\partial q}{\partial t}\right)_{adv}, \quad (3)$$

where ε_{ci} is the integral deposition/sublimation rate, $(L_i/c_p)\varepsilon_{ci}$ is the latent heating rates of deposition/evaporation, $(L_f/c_p)\varepsilon_{fr}$ and $(L_m/c_p)\varepsilon_m$ are the freezing/melting heating rates, $(\partial T/\partial t)^{rad}$ is the radiative heating rate, and the last terms represent the advective tendencies obtained from the ECMWF analyses.

Expressions for the integral condensation ε_{c1} and deposition ε_{c2} growth rates are written following KC99a and KS98a:

$$\varepsilon_{ci}=4\pi\rho_i\int_0^\infty \dot{r}_i' r_i'^2 f_i dr_i=\frac{4\pi D'\rho_a' k_{fi}'\delta_i'}{Q_i\xi_i^2}\int_0^\infty r_i f_i dr_i$$
$$=(4\pi D' N_i\bar{r}_i)\delta_i\frac{k_{fi}}{Q_i\xi_i^2}=\frac{\delta_i'}{\tau_{fi}}\frac{k_{fi}}{Q_i\xi_i^2}\approx\frac{\delta_i}{\tau_{fi}}. \quad (4)$$

where δ is the supersaturation. Supersaturation relaxation times for droplets τ_{f1} and for crystals τ_{f2} are defined as

$$\tau_{fi}=(4\pi D N_i\bar{r}_i)^{-1}; \quad (5)$$

$\tau_f=\tau_{f1}$ for pure liquid cloud and $\tau_f=\tau_{f2}$ in pure crystalline clouds. The supersaturation relaxation times for droplets τ_{f1} and for crystals τ_{f2} given by (5) are the characteristic times of supersaturation to decrease by a factor of e, if supersaturation generation is absent. Note that these times are very different for liquid clouds, τ_{f1} ~1-10 s [Sedunov, 1974], and for crystalline clouds, τ_{f1} ~0.5-5 hours and more (KS98b; KS00). Value τ_f in mixed cloud has intermediate values, from a few seconds to a few hours.

The system of equations for thermodynamics and microphysics is solved by the splitting method as described in K95 and KS98a. At the first substep of splitting, the fields of T, q, and $f_i(r_i)$ at one model time step Δt are calculated during the transport along the z axis by vertical velocities and turbulence. During the next step of splitting, after removal of space variables, a Lagrangian zero dimensional problem is solved, equivalent to the parcel model. Equations for the temperature and humidity can be written in the form

$$\frac{dT}{dt} = \frac{L_1}{c_p}\varepsilon_{c1} + \frac{L_2}{c_p}\varepsilon_{c2} - \gamma_a\left(w + w_{\text{rad}}\right); \quad \frac{dq}{dt} = -\varepsilon_{c1} - \varepsilon_{c2}, \tag{6}$$

where c_p is the specific heat capacity, L_i is the condensation or sublimation heat, γ_a is the dry adiabatic lapse rate. The "effective radiative velocity" $w_{\text{rad}} = -(1/\gamma_a)(\partial T/\partial t)^{\text{rad}}$ is introduced following KC99a, which allows the simple comparison of dynamical and radiative effects.

Differentiating supersaturation $\delta_1 = q - q_{s1}$ with respect to time and substituting (6), we obtain

$$\begin{aligned}\frac{d\delta_1}{dt} &= \frac{dq_{s1}}{dt} - \frac{\partial q_{s1}}{\partial t}\frac{dT}{dt} = -\left(\varepsilon_{c1} + \varepsilon_{c2}\right) \\ &\quad - \frac{\partial q_{s1}}{\partial t}\left(\frac{L_1}{c_p}\varepsilon_{c1} + \frac{L_2}{c_p}\varepsilon_{c2} - \gamma_a\left(w + w_{\text{rad}}\right)\right) \\ &= -\varepsilon_{c1}\left(1 + \frac{L_1}{c_p}\frac{\partial q_{s1}}{\partial T}\right) - \varepsilon_{c2}\left(1 + \frac{L_2}{c_p}\frac{\partial q_{s1}}{\partial T}\right) + \frac{\partial q_{s1}}{\partial T}\gamma_a\left(w + w_{\text{rad}}\right)\end{aligned} \tag{7}$$

Substituting (4) for ε_{c1}, ε_{c2} and using the relation $\delta_2 = \delta_1 + (q_{s1} - q_{s2})$, we derive an equation for supersaturation δ_1 for the three-phase system, containing water vapor, droplets, and crystals:

$$\begin{aligned}\frac{d\delta_1}{dt} &= -\left(\frac{\beta_1}{\tau_{f1}} + \frac{\beta_2}{\tau_2}\frac{Q_{21}}{Q_2}\right)\delta_1 - \beta_2\frac{Q_{21}}{Q_2}\tau_{f1}^{-1}\left(q_{s1} - q_{s2}\right) \\ &\quad + \frac{\partial q_{s1}}{\partial T}\gamma_a\left(w + w_{\text{rad}}\right),\end{aligned} \tag{8}$$

where $\beta_1 = k_{f1}/\xi_1^2$, $\beta_2 = k_{f2}/\xi_2^2$ ($\beta_i = 1$ for spheres), and $Q_1 = 1 + (L_1/c_p)(\partial q_{s1}/\partial T)$, $Q_{21} = 1 + (L_2/c_p)(\partial q_{s1}/\partial T)$. The last term of (8) with w_{rad} accounts for the radiative effects on supersaturation, on the growth rates of individual droplets and crystals.

Equation (8) describes three processes governing the supersaturation budget. The first term on the right-hand side of (8) describes relaxation of supersaturation due to absorption of the vapor by droplets and crystals. The second term describes distillation of water vapor from droplets to crystals because saturated humidity over the ice is lower than humidity over the water, thus this term is proportional to the difference $q_{s1}(T) - q_{s2}(T)$ (Bergeron-Findeisen mechanism). The third term on the right-hand side of (8) describes generation of supersaturation due to rising motion or radiative cooling, or depletion of supersaturation if $(w + w_{\text{rad}}) < 0$.

In the same way, equations for the ice supersaturation δ_2 and for the temperature T can be obtained:

$$\begin{aligned}\frac{d\delta_2}{dt} &= -\left(\frac{Q_{21}}{Q_2}\tau_{f1}^{-1} + \beta_2\tau_{f2}^{-1}\frac{Q_{21}}{Q_2}\right)\delta_2 + \beta_2\frac{Q_{21}}{Q_2}\tau_{f2}^{-1}\left(q_{s1} - q_{s2}\right) \\ &\quad + \beta_2\frac{\partial q_{s2}}{\partial T}\gamma_a\left(w + w_{\text{rad}}\right),\end{aligned} \tag{9}$$

$$\frac{dT}{dt} = \left(\frac{\lambda_1}{Q_1}\tau_{f1}^{-1} + \frac{\lambda_2}{Q_2}\tau_{f2}^{-1}\right) + \frac{\lambda_2}{Q_2}\tau_{f2}^{-1}\left(q_{s1} - q_{s2}\right) - \gamma_a\left(w + w_{\text{rad}}\right), \tag{10}$$

where $\lambda_i = L_i/c_p$.

4. Results

The simulations described in this section used a model vertical domain of 12 km, with 31 grid points separated by an interval of 400 m. The main time step is 10 s, with smaller time steps used as needed in the condensation subroutines to ensure computational stability.

4.1. Model Initialization

The radar data on July 8 (Plate 1) show the existence of a lower cloud layer at 2-5 km and formation of the upper layer at 1030 UTC. The radiosonde profiles of temperature and relative

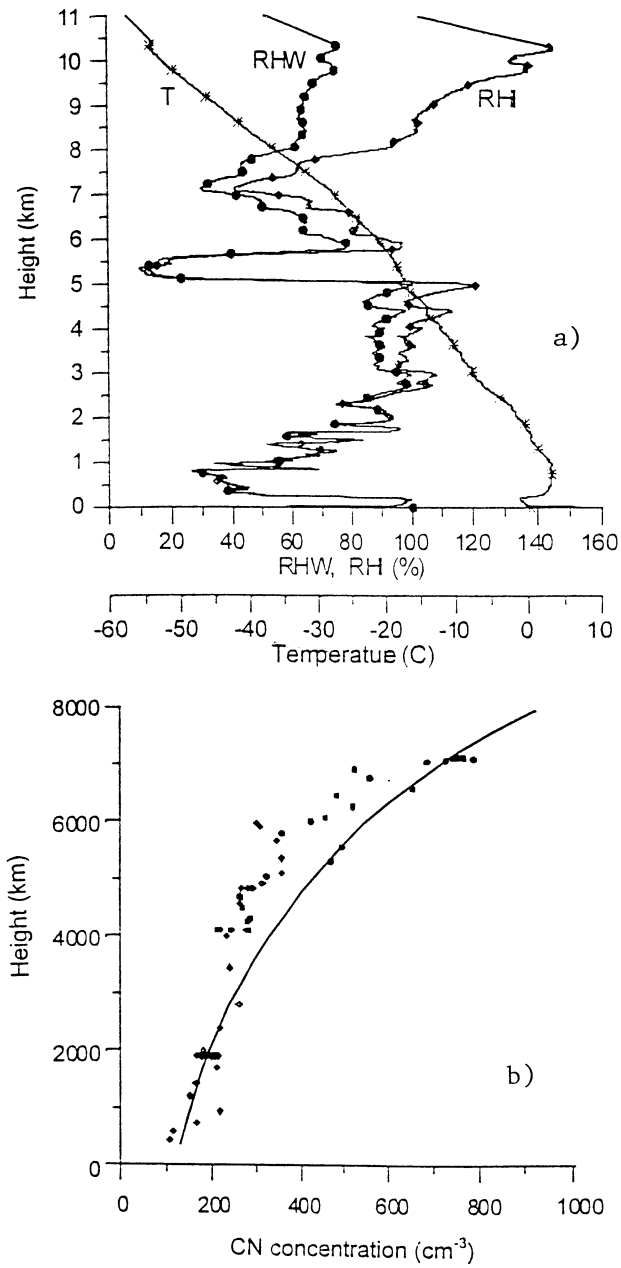

Figure 2. Vertical profiles measured (in situ) on July 8, 1998, at the SHEBA site: (a) sounding data at 1110 UTC of temperature (T), relative humidity over water (RHW), and over ice (RHI); and (b) condensation nuclei measured from aircraft around 2130 UTC (dots) and initial profile used in simulations (solid curve).

humidity (1110 UTC) over water (RHW), and ice (RHI), are shown in Figure 1, and the vertical profiles of condensation nuclei (CN) measured with aircraft between 2100 and 2300 UTC are shown in Figure 2. The initial profile of CN was constructed using an exponential function matching the measured values as shown in Figure 2. The values of RHW are slightly less than 100% in the layer 3-5 km. The upper layer 8-10.5 km exhibits high supersaturation with respect to ice with maximum δ_i = 144% at 10.5 km, while δ_w = -35-40% in this layer.

To initialize the model, the sounding profiles from SHEBA site at 1110 UTC were interpolated from the irregular sounding height mesh to the regular mesh of the model. The vertical profiles of the temperature and humidity advection were taken from the hourly ECMWF data that were archived for SHEBA *[Beesly et al., 2000]*. The hourly advective tendencies were kept constant during each 1 hour of simulation.

The simulation using the observed initial conditions and advective tendencies did not produce a cloud that was at all similar to the observed one. The upper cloud did not form until 1500 UTC (as described in more detail in section 4.3). Because of the sensitivity of ice nucleation to the relative humidity, small errors in the radiosonde measurements can adversely affect the simulations. Radiosondes are not capable of measuring small supersaturations with respect to water. Additionally, the accuracy of radiosonde humidity measurements decreases significantly at temperatures below -40°C. The ECMWF advective tendencies are also subject to errors. The only radiosonde in the Arctic Ocean during this period was at the SHEBA site: hence the ECMWF simulations of large-scale dynamics in the region are not well-constrained by observations. Comparison of ECMWF with aircraft-derived advective tendencies at 2200 UTC show substantial discrepancies. An additional factor was that the ECMWF advective tendencies did not include condensed water. Because of the uncertainties in the radiosonde humidity measurements and the advective tendencies, the data set cannot be used unambiguously to "validate" the model parameterizations. Rather, we use the data set, and perturbations of the observations, to explore the formation and evolution mechanisms of the cloud system through the simulations. To reproduce the cloud conditions during the period 1100-1200 UTC, it was found that the following perturbations of humidity and vertical velocity were required: (1) increase RHI in the layer 8.5-10.5 km by 15% and (2) increase RHW by 5-10% at z = 2.5-5 km such that the initial RHW = 0.99. We also impose a perturbation of the ECMWF vertical velocity such that the modified value is $w \sim 0.5$-1 cm s^{-1} in the layer between 2.5 and 5 km, and $w \sim 0.5$-2.5 cm s^{-1} in the layer between 2.5 and 5 km. Such perturbations are required since the model does not include a parameterization of sub-grid-scale motions above the boundary layer.

With these modifications to the relative humidity and vertical velocity, a cloud system similar to the observed one was formed. We describe first the "control" run and then describe the model sensitivity tests to the initial RHW and nucleation schemes. The ice nucleation schemes in the control run are the following: (1) activation of droplets is allowed if water supersaturation becomes positive; (2) heterogeneous nucleation of crystals according to MDC92 parameterization is allowed at temperatures higher than -20°C; and (3) homogeneous ice nucleation is allowed at negative temperatures.

4.2. Control Simulation

The modeled height-time display of cloud development with adjusted initial conditions is presented in Plate 2. Cloud formation in both layers starts after 15-20 minutes of simulation time, but the formation mechanisms are completely different in lower As and upper Ci.

4.2.1. As formation and dissipation. Because of the positive vertical velocity, the simulated water supersaturation becomes positive in less than a quarter of an hour (Plate 2a) and the condensation in the lower layer begins initially at a height of 3 km (Plates 2b, 2c, 2d). Throughout the simulation, LWC does not exceed 0.16 g m^{-3}, and droplet concentration is rather low with a maximum value of 14 cm^{-3}. The low number concentration of liquid drops arises from the mixed-phase nature of this cloud layer and operation of the Bergeron-Findeisen process that causes evaporation of small droplets, a decrease in droplet concentration and an increase in mean radius (Plate 2d). The simulated crystal concentration is rather low, 1-3 L^{-1} (Plate 2f), because the two mechanisms of crystal formation acting here are not very effective: droplet freezing is rather slow due to the relatively high temperature (about -10°C and heterogeneous ice nucleation by MDC92 scheme is slow since δ_i < 3-5%.

Hence a relative equilibrium between liquid drop nucleation and depletion by freezing is established, and the *As* cloud exists in mixed phase for almost 3 hours. Then the cloud gradually glaciates and the liquid phase vanishes by 1300 UTC, mostly due to the seeding from the Ci layer aloft and because the supersaturation over water becomes negative and new droplets cannot form. The simulated cloud phase is in agreement with the surface microwave radiometer measurements of liquid water path (LWP), which shows a minimum of column LWP less than 0.018 kg m^{-2} at 1100 UTC, an increase to 0.040 kg m^{-2} by 1300 UTC, and almost zero after 1400-1500 UTC. The lower boundary of the cloud is located at the height of 2 km during this entire period, coinciding with the 0° isotherm where ice crystals melt, and the drops rapidly evaporate in the underlying dry layer.

The maximum crystal concentration (57 L^{-1}, Plate 2f) is reached at 1040 UTC due to nucleation impulse at the height of 10 km after relative humidity exceeds a threshold value (the threshold RHI are given by *Sassen and Dodd* [1989]. The maxima of IWC (25 mg m^{-3}, Plate 2g), crystal radii (100-120 μm, Plate 2h), radar reflectivity (0-3 dBz, Plate 2i) and fall velocity (0.9 m s^{-1}, Plate 2j) are reached in the *As* layer by 1300 UTC, due to crystal growth in supersaturated environment (Plate 2e), in good agreement with the radar measurements (Plate 1). Since the formation of the liquid phase is suppressed after 1300-1400 UTC (supersaturation with respect to water is negative at all heights after 1300 due to presence of crystals and their absorption of water vapor), and the large crystals precipitate, the *As* gradually dissipates, which is seen as the uplift of the lower boundary after 1300-1400 UTC.

4.2.2. Upper cirrus formation and periodical renewal. The most interesting and characteristic feature of this cloud system seen in radar (Plate 1) is the periodical formation of *Ci* layers at 9-11 km and their descent down to heights of 4-5 km. Such behavior was explained for the first time by *Sassen and Dodd* [1988, 1989] using a parcel model, which showed that this periodicity may be caused by impulses of homogeneous freezing of the deliquescent submicron particles of ammonium sulfate. This mechanism appears to be a fundamental feature of cirrus formation.

The ice supersaturation δ_i in the control run reached a maximum 60%, corresponding to RHW values of 60-75%. This means that ammonium sulfate, which has a threshold of deliquescence of 80%, could not serve as haze particles for homogeneous freezing (assuming that these particles have not been processed by the cloud, which would lower the deliquescence threshold). So in the absence of heterogeneous freezing and deliquescent ammonium sulfate haze, the only possible nucleation mechanism is homogeneous freezing of sulfuric acid particles, which have a much lower deliquescent threshold.

The cirrus cloud in the control run forms initially at about 1030 UTC at 10 km (Plates 2e-2h), in agreement with radar observations (Plate 1). The crystal concentration reaches a maximum of 57 L^{-1} at 1100 UTC at z = 10 km (Plate 2), the IWC reaches its maximum value 11 mg m^{-3} by 30 min later at z = 8.5-9 km (Plate 2g) and crystal mean radius reaches here 60-70 μm (Plate 2h). This lag of IWC and radius behind the ice crystal concentration is explained by the values of supersaturation relaxation times, which are here ~100 min (Plate 2k). After the nucleation impulse, supersaturation decreases due to vapor absorption by the crystals, humidity drops below the threshold value, and a new nucleation is prohibited for some time. Ice crystals formed during the initial impulse precipitate, grow and form a descending plume, which is seen in the height-time display (Plates 2f-2h). This plume merges with the underlying mixed-phase As at 1300-1330 UTC as also shown in radar Plate 1, effectively "seeding" the original *As*.

After fallout of the crystals from the cirrus-generating layer at ~10 km, the supersaturation begins to increase, and finally, a threshold supersaturation value is reached so that a new nucleation impulse occurs, and the entire chain of events is repeated periodically. In the control run, two secondary nucleation impulses occur at 1530 and 2100 UTC at 10-10.5 km (Plate 2g), which is also in good agreement with radar observations (Plate 1a). The plumes from these two impulses precipitate similar to the first one. A remarkable feature of this *Ci* cloud is a residual supersaturation over ice -30-40% at 8-11 km (Plate 2e), since the ice crystal supersaturation absorption time τ_{fc} is 120-300 min in the main cirrus layer (Plate 2k). Thus the vapor excess (VE) (uncondensed ice supersaturation in cloud) reaches 40-75 mg m^{-3}, which is comparable or substantially greater than the amount of condensed ice, i.e., IWC (Figure 2g). The relative amount of condensed ice defined as RACI=IWC/(IWC+VE) does not exceed 20-50% most of the time with the only exception 75% at 8-10 km in the third nucleation impulse after 2100 (Plate 2l). This RACI characterizes the difference between this explicit microphysical approach with the evaluation of supersaturation and a bulk model where all or almost all supersaturation is condensed, so the residual $\delta_i \sim 0$ and RACI would be -100%. In the explicit approach, RACI << 100%, and the optical thickness and latent heat of deposition are much smaller (by a factor of 3-10 in various portions of the cloud) than they would be in a bulk model with condensation at a relative humidity of 100%.

The nucleation impulses were discussed in detail in KS98a and KSOI with respect to midlatitude cirrus, showing that the condensation process is slow there. The agreement of Plate 2 (simulation) and Plate 1 (radar observations) shows that this polar cirrus cloud exhibits similar properties. Thus the main features of the polar cirrus layer observed on July 8 are: (1) its impulselike formation and development as predicted by *Sassen and Dodd* [1988, 1989], based on the hypothesis of the dominant role of homogeneous nucleation; and (2) slow condensation and relatively small amount of ice.

Aircraft flights were performed over the SHEBA site at around 2130 UTC. Simulated profiles of the crystal concentration, IWC, and mean particle radius are compared in Figure 3 with those obtained with aircraft observations and from cloud radar. The model data are averaged from hour 24 of the simulation which is valid at the time of the observations. The simulated profiles were obtained one hour after a strong nucleation impulse occurred in the model between 10 and 11 km. The modeled cloud layer is much deeper than observed, extending above and below the observed cloud top and base, respectively (Figure 3a). Part of this discrepancy may be explained by the inability of the cloud radar to detect small ice crystals aloft. The maximum modeled IWC of 0.066 g m^{-3} is somewhat greater than the maximum value of 0.039 g m^{-3} in the median radar profile and much greater than the mean values observed in situ with the CPI probe. The range of IWCs obtained with the CPI are indicative of the large horizontal variations in the cloud ice mass.

The modeled ice crystal concentrations (10-15 L^{-1}) are much smaller than those observed with the CPI (300-400 L^{-1}) (Figure 3b). Examination of the CPI images revealed that the ice crystal size distribution was dominated by small spherical crystals, indicating that the particles may have recently formed via condensation freezing. Additional analyses of the aircraft microphysics data revealed that small amounts of liquid water were present in the cloud as late as 2200 UTC, bolstering the idea that condensation freezing had recently occurred in the cloud. Seeding of the liquid water layer by ice crystals aloft could have produced the large concentrations of small ice crystals observed by the CPI. The modeled mean ice particle sizes are about 30% larger than that retrieved with radar and 10 times larger than that observed with the CPI (Figure 3c). The modeled and observed vertical distribution of ice particle size are similar, with the larger particles being found near cloud base. This trend is easily seen in the radar data and the maximum of the CPI particle size ranges.

The most notable disagreements among the model, radar, and CPI observations are in the profiles of ice crystal concentration and size. The crystal concentrations observed with the CPI are 1 order of magnitude greater than the modeled values and typically observed in synoptic-scale cirrus of a few crystals per liter [e.g., *Sassen et al.* 1989; *Jensen et al.*, 1994; *Heymsfield and Miloshevich*, 1995], with many small spherical particles being detected possibly indicating recent condensation freezing. This discrepancy may be caused by the following reasons:

1. The presence of liquid drops formed in the small-scale updrafts are not adequately treated in the single-column version of the model or adequately observed via surface-based instrumentation. In agreement with the surface-based measurements the modeled liquid layer has long since been depleted (Plate 2); however, several probes on the C-130, notably the icing rate detector, indicate that small quantities of water are still present as late as 2200 UTC. The persistence of liquid in the cloud layer allows for a high concentration of small ice particles as crystals from above continue the seeder-feeder process for a much longer period than modeled.

2. A single-column version of the model is based on the large-scale dynamic forcing with vertical velocities of a few cm s^{-1} and does not account for the small-scale updrafts of the

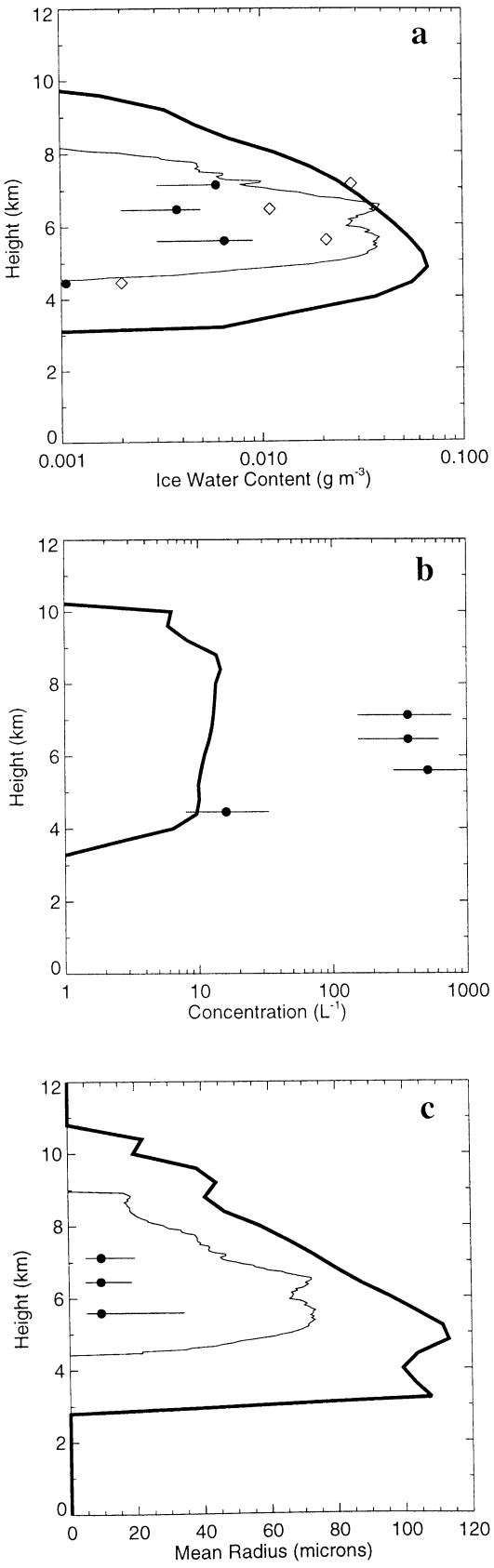

Figure 3. Comparison of the simulated (solid curve) versus observed at 2200 UTC values of (a) ice water content, (b) ice crystal concentration, and (c) mean crystal radius. Diamonds represent maximum IWC obtained with the CPI probe during the leg. Observations from CRI probe (circles) and radar (dashed curve).

order of 0.5 m s^{-1} which can lead to the nucleation of the new droplets at appropriate situations of increased instability. These situations should be modeled with 2-D or 3-D models, or the subgrid updrafts and nucleation should be parameterized in the single-column models.

4.3. Sensitivity Studies

As discussed in section 1, a major uncertainty in the simulation of cirrus clouds is parameterization of ice crystal nucleation. Here we examine the impact of different nucleation schemes. Because of the sensitivity of these nucleation schemes to relative humidity, we also examine the impact of varying the initial humidity.

Plate 3 shows the simulated cloud development using the observed sounding profile of RHW as is shown in Figure 1 (i.e., without being adjusted as in the control run). The picture is essentially different from the control run and radar observations. Only 1-3 L^{-1} crystals form at the beginning in a very thin layer above 8 km. The first nucleation impulse at 1100 UTC which was precipitating and merging with *As* in the control run is absent in this simulation. Since the supersaturation generation occurs slowly in the presence of weak updrafts and advective forcing, the first noticeable nucleation impulse occurs at 1300 UTC, and only by 1500-1800 UTC does the simulation resemble the control run. However this "spin-up" due to the underestimation of the humidity by the sounding at low temperatures takes 6-8 hours. This run demonstrates the necessity for improvements to the sounding humidity measurements at low temperatures and shows that present observations are of insufficient accuracy to verify the modeled nucleation parameterizations. An additional issue is the boundary advection of ice water into the column, which is assumed here to be zero (and is not specified in the ECMWF analyses).

Plate 4 shows the simulated cloud using the same initial humidity profile as in the control run, but in addition to homogeneous nucleation, heterogeneous nucleation was also allowed in the cirrus layer, described by the MDC92 method with exponential dependence on ice supersaturation. Crystal nucleation starts just at the beginning with concentrations reaching 57 L^{-1}. The simulated crystals are smaller in size than in the control run and form in a very thin layer, so precipitation from the first plume evaporates in the dry layer at 5-6 km and does not completely merge with the *As* layer. However, the most significant difference with the control run is that crystal nucleation is not impulse-like as in the control run. The first ice crystal concentration maximum at 1030 UTC is caused by homogeneous nucleation. Then, heterogeneous nucleation (which does not require a threshold humidity), acts continuously and decreases the supersaturation below the threshold of homogeneous nucleation. Thus, heterogeneous nucleation suppresses the homogeneous nucleation and the entire crystal formation process becomes continuous instead of showing the impulses that are characteristic of homogeneous nucleation. The crystal concentration (Plate 4a) is much smaller than the initial aerosol concentration; therefore no special corrections were made for the CCN change due to crystal nucleation. The crystal concentration remains constant with time after 1400 UTC, although IWC is still modulated by the changes in advective forcing and vertical velocities. Similar results on possible suppression of homogeneous mode by acting heterogeneous nucleation were obtained by *DeMott et aL* [1994].

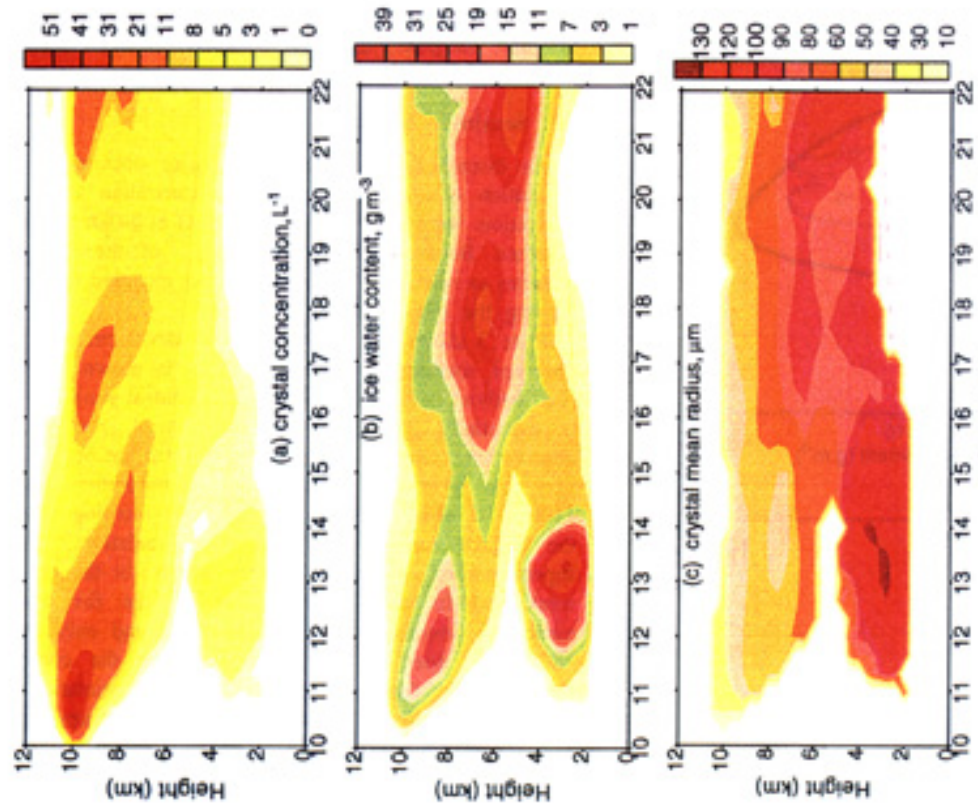

Plate 3. Sensitivity to the initial humidity. Simulated cloud evolution in the run with original (unmodified) sonde humidity profiles: (a) crystal concentration, L^{-1}; (b) ice water content, mg m^{-3}; (c) crystal mean radius, μm.

Plate 4. Simulation with heterogeneous nucleation allowed in the cirrus layer: (a) crystal concentration, L^{-1}; (b) ice water content, mg m^{-3}; (c) crystal mean radius, μm; (d) ice supersaturation, %.

Several additional simulations were performed with the other heterogeneous nucleation schemes, in particular, with the Fletcher-type temperature dependence. For each of these simulations, heterogeneous nucleation suppressed homogeneous crystal nucleation, and the modeled cloud was different from the observed one. These simulations imply that only homogenous nucleation occurs in the upper levels of the cloud, which gives rise to the periodicity in ice crystal concentration seen in the radar images.

5. Conclusions

A cloud model, including kinetic equations for. the droplet and crystal size distribution functions and the supersaturation equation, was used to simulate the case study of July 8 1998, observed during the SHEBA campaign. The time period 1000-2200 UTC was simulated, when a two-layer cloud system consisting of *As* and *Ci* was observed to merge into a single cloud layer. The cloud microphysical observations for this case included a time series of radar reflectivities and Doppler velocities (from which ice crystal microphysical properties were retrieved) and aircraft in situ measurements of cloud microphysical properties made with the Cloud Particle Imager.

The model was run in "single-column" mode, using hourly values of the temperature and humidity advection and large-scale vertical velocities obtained from ECMWF analyses. Since the process of cloud formation is sensitive to the initial humidity and mechanisms of nucleation and dynamical forcing, these characteristics were varied in the model sensitivity runs to obtain the best agreement with the observational data and to test the model sensitivity to the variation of the initial humidity and nucleation schemes. The simulation using the observed sounding humidity produced a cloud system very different from that observed: in the early part of the simulation, cirrus was strongly suppressed and the model spin-up (the time before simulation results became similar to observations) was 6-8 hours. To produce a simulation similar to the observed clouds, the initial values of RHW had to be increased by 15%. While errors in the radiosonde relative humidity are expected, it is not clear how much of the required adjustment to the humidity profile was associated with the sounding errors and how much might reflect deficiencies in the model. An additional contributing factor is neglect of ice water advected into the column. It is unfortunate that the radiosonde humidity observations were of insufficient accuracy to provide an unambiguous test of the model and that ice water advection was unavailable. The best nucleation scheme included: (1) heterogeneous activation of droplets at positive water supersaturation; (2) heterogeneous ice nucleation at temperatures warmer than -35°C only; and (3) only homogeneous nucleation by freezing of sulfuric acid droplets in cirrus layer at temperatures colder than -40°C.

Under these conditions a two-layer cloud system formed in the control model run at 1030 UTC, consisting of mixed-phase *As* at 2-5 km and crystalline cirrus at 9-10 km. The cirrus layer slowly precipitated and merged with the underlying *As* at 1300-1330 UTC, seeding the *As* and causing its complete crystallization. The lower *As* layer gradually precipitated and its lower boundary lifted by 1 km. In the upper cirrus-generating layer at 9-11 km, there were several additional impulses of crystal formation with time intervals 3-4 hours, which formed precipitation and resulted in a vertically extended cirrus layer up to 6 km thick with the lower boundary at 4 km. This impulse-like periodic formation of crystals due to homogeneous nucleation was suggested by *Sassen and Dodd* [1988, 1989] to be an important mechanism for cirrus formation. Our simulations indicate that the Sassen-Dodd effect may be responsible for the maintenance of the July 8 cirrus for at least 12 hours and may explain the evolving structure of the cloud system seen in the radar images.

The simulated vertical profiles of crystal concentration and mean crystal radius differ from observations in several key areas. The modeled ice crystal concentrations are much smaller that observed with the Cloud Particle Imager (CPI) while the modeled mean crystal size is much larger than observed by both the radar and the CPI. This may be due to the presence of recently frozen cloud droplets in the CPI observations or it may suggest that the model is deficient in accounting for small ice crystals. In addition, the use of large-scale vertical velocities in the model may not be adequate for simulating the microstructure of cirrus as mesoscale motions may locally enhance nucleation significantly [*Meyers et al.*, 1992; *Khvorostyanov and Sassen*, 1998, 2000].

These results provide insight for understanding the mechanisms of cloud formation and ice particle nucleation in middle and upper level clouds in the Arctic, including mixed-phase clouds. This insight can be used in the development of suitable parameterizations for Arctic clouds to be used in large-scale models. Assessment of the generality of these results will require analysis and simulation of additional cases.

Acknowledgments. This research was supported by NASA FIRE and DOE ARM. We would like to thank T. Uttal, S. Matrasov, and the anonymous reviewers for their comments on the manuscript.

References

Beesley, J. A., C. S. Bretherton, C. Jakob, E. L Andreas, J. M. Intrieri, and T. A. Uttal, A comparison of cloud and boundary layer variables in the ECMWF forecast model with observations at Surface Heat Budget of the Arctic Ocean (SHEBA) ice camp, *J Geophys. Res.*, *105*, 12,337-12,349, 2000.

Buikov, M. V., V. I. Khvorostyanov, Numerical simulation of radiation fog and stratus formation taking into account interaction among dynamical, radiative and microphysical processes, *Proc. Int. Cloud Phys. Conf. 6th*, 392-396, 1976.

Curry, J. A., F. G. Meyer, L. F. Radke, C. A. Brock, and E. E. Ebert, Occurrence and characteristics of lower tropospheric ice crystals in the Arctic, *Int. J Climatol.*, *10*, 749-764, 1990.

Curry, J.A., J. Schramm, and E.E. Ebert, Impact of clouds on the surface radiation budget of the Arctic Ocean, *Meteorol. Atmos. Phys.*, *51*, 197-217, 1993.

Curry, J. A., W. B. Rossow, D. Randall, and J. L. Schramm, Overview of Arctic cloud and radiation properties, *J. Clim.*, *9*, 1731-1764, 1996.

Curry, J.A., et al., FIRE Arctic Clouds Experiment, *Bull. Am. Meteorol. Soc.*, *81*, 5-29, 2000.

DeMott, P. J., M. P. Meyers, and W. R. Cotton, Parameterization and impact of ice initiation processes relevant to numerical model simulation of cirrus clouds, *J. Atmos. Sci.*, *51*, 77-90, 1994.

Fletcher, N. H., *The Physics of Rainclouds*, 390 pp., Cambridge, Univ. Press, New York, 1962.

Fowler, L. D., D. A. Randall, and S. A. Rutledge, Liquid and ice cloud microphysics in the CSU general circulation model, part 1, Model description and simulated microphysical processes, *J. Clim.*, *9*, 489-529, 1996.

Girard, E., and J. -P. Blanchet, Microphysical parameterization of Arctic diamond dust, ice fog and thin stratus in climate models, *J. Atmos. Sci.*, in press, 2000.

Girard, E., and J. A. Curry, Simulation of Arctic low-level clouds observed during the FIRE Arctic Clouds Experiment using a new bulk microphysics scheme, *J. Geophys. Res.*, this issue.

Heymsfield, A. J., and L. M. Miloshevich, Relative humidity and temperature influences on cirrus formation and evolution, Observations from wave clouds and FIRE-II, *J. Atmos. Sci., 52*, 4302-4303, 1995.

Heymsfield, A. J., and R. M. Sabin, Cirrus crystal nucleation by homogeneous freezing of solution droplets, *J. Atmos. Sci., 46*, 2252-2264, 1989.

Hobbs, P. V., and A. L. Rangno, Microstructures of low and middle-level clouds over the Beaufort Sea, *Q. J. R. Meteorol. Soc., 124*, 2035-2071, 1998.

Jensen, E. J., 0. B. Toon, D. L. Westphal, S. Kinne, and A. J. Heymsfield, Microphysical modeling of cirrus, 1, Comparison with 1986 FIRE IFO measurements, *J. Geophys. Res., 99*, 10,421-10,442, 1994.

Jiang, H., W. R. Cotton, J. 0. Pinto, J. A. Curry, and M. J. Weissbluth, Sensitivity of mixed-phase Arctic stratocumulus to ice forming nuclei and large-scale heat and moisture advection, *J. Atmos. Sci., 57*, 582-594, 2000.

Khvorostyanov, V. I., Two-dimensional time-dependent microphysical model of low clouds and fogs, *Sov. Meteorol. Hydrol., 7*, 16-28, 1982.

Khvorostyanov, V. I., Mesoscale processes of cloud formation, cloud-radiation interaction and their modelling with explicit microphysics, *Atmos. Res., 39*, 1-67, 1995.

Khvorostyanov, V. I., and J. A. Curry, A simple analytical model of aerosol properties with account for hygroscopic growth. 1, Equilibrium size spectra and CCN activity spectra, 2, Scattering and absorption coefficients, *J. Geophys. Res., 104*, 2163-2174, 2175-2184, 1999a.

Khvorostyanov, V. I., and J. A. Curry, Towards the theory of stochastic condensation in clouds, part 1, A general kinetic equation, part 2, Analytical solutions of gamma distribution type, *J. Atmos. Sci., 56*, 3985-3996, and 3997-4013, 1999b.

Khvorostyanov, V. I , and J. A. Curry, A new theory of heterogeneous nucleation for application in cloud and climate models, *Geophys. Res. Lett, 27*(24), 4081-4084, 2000.

Khvorostyanov, V. I., and K. Sassen, Cirrus cloud simulation using explicit microphysics and radiation, part 1, Model description, *J. Atmos. Sci., 55*, 1808-1821, 1998a.

Khvorostyanov, V. I., and K. Sassen, Cirrus cloud simulation using explicit microphysics and radiation, Part 2, Microphysics, vapor and ice mass budgets, and optical and radiative properties, *J. Atmos. Sci., 55*, 1822-1845, 1998b.

Khvorostyanov, V. I., and K. Sassen, Towards the theory of homogeneous nucleation and its parameterization for cloud models, *Geophys. Res. Lett., 25*(16), 3155-3158, 1998c.

Khvorostyanov, V. I., and K. Sassen, Microphysical processes in cirrus and their impact on radiation, a mesoscale modeling perspective, in *Collective Monograph "Cirrus,"* Oxford Univ. Press, New York, in press, 2001.

Korolev, A. V., G. A. Isaac, J. Hallett, Ice particle habits in Arctic clouds, *Geophys. Res. Lett., 26*, 1299-1302, 1999.

Lawson, R. P. and B. A. Baker, and C. G. Schmitt, Overview of microphysical properties of Arctic clouds observed in May and July 1998 during FIREACE, *J. Geophys. Res.*, this issue.

Liljegren, J., Observations of integrated water vapor and cloud liquid water at SHEBA, in *Proceedings of the Ninth Annual ARM Science Team Meeting,* Atmos. Radiat. Meas., Dep. of Energy, Washington, D.C., 1999.

Matrosov, S. Y., B. W. Orr, R. A. Kropfli, and J. B. Snider, Retrieval of vertical profiles of cirrus cloud microphysical parameters from Doppler radar and infrared radiometer measurements, *J. Appl. Meteorol., 33*, 617-626, 1994.

Perovich, D. K., et al., Year on ice gives climate insights, *EOS Trans. AGU, 80*(41), 481, 485-486, 1999.

Pinto, J. 0., Autumnal mixed-phase cloudy boundary layers in the Arctic. *J. Atmos. Sci., 55*, 2016-2038, 1998.

Pinto, J. 0., J. A. Curry, and J. M. Intrieri, Cloud-aerosol interactions during autumn over the Beaufort Sea, *J. Geophys. Res.*, this issue.

Pruppacher, H. R., and J. D. Klett, *Microphysics of Clouds and Precipitation,* 997 pp., 2nd ed, Kluwer Acad., Norwell, Mass., 1997.

Randall, D. A., and D. G. Cripe, Alternative methods for specification of observed forcing in single-column models and cloud system models, *J. Geophys. Res., 104*, 24,527-24,545, 1999.

Randall, D. A, K. M. Xu, R. J. C. Somerville, and S. Iacobellis, Single-column models and cloud ensemble models as links between observations and climate models, *J. Clim., 9*, 1683-1697, 1996.

Rogers, D. C., P. J. DeMott, and S. M. Kreidenweis, Airborne measurements of tropospheric ice nucleating aerosol particles in the Arctic spring, *J. Geophys. Res.*, this issue.

Sassen, K., Ice nuclei availability in the higher tropospheric, implications of a remote sensing cloud phase climatology, in *Nucleation and Atmospheric Aerosols,* edited by N. Fukuta and P. Wagner, pp. 287-290, A. Deepak, Hampton, Va., 1992.

Sassen, K., and G. C. Dodd, Homogeneous nucleation rate for highly supercooled cirrus cloud droplets, J. Atmos. Sci., *45*, 1357-1369, 1988.

Sassen, K., and G. C. Dodd, Haze particle nucleation simulation in cirrus clouds, and application for numerical and lidar studies, *J. Atmos. Sci., 46*, 3005-3014, 1989.

Sassen, D., O'C. Starr, and T. Uttal, Mesoscale and microscale structure of cirrus clouds, Three case studies, *J. Atmos. Sci., 46*, 371-396, 1989.

Sedunov, Y. S., *Physics of Drop Formation in the Atmosphere,* 234 pp., John Wiley, New York, 1974.

Shupe, M. D., T. Uttal, S. Y. Matrosov, and A. S. Frisch, Cloud water contents and hydrometeor sizes during the FIRE Arctic Clouds Experiment, *J. Geophys. Res.*, this issue.

Yum, S. S., and J. G. Hudson, Vertical distributions of cloud condensation nuclei spectra over the springtime Arctic Ocean, *J. Geophys. Res.*, this issue.

B.A. Baker, SPEC, Inc., Boulder, CO 80301.

J.A. Curry, V.I. Khvorostyanov, and J.O. Pinto, Department of Aerospace Engineering Sciences, UCB 429, University of Colorado, Boulder, CO 80309-0429. (curryja@cloud.colorado.edu; 2318.g23@g23.relcom.ru; pinto@monsoon. colorado.edu)

K. Sassen, University of Utah, Salt Lake City, UT 84112-0111.

M. Shupe, Science and Technology Corporation, NOAA, Environmental Technology Laboratory, Boulder, CO.

(Received December 22, 1999; revised June 16, 2000;
accepted June 27, 2000.)